The role of microstructure in crack growth during liquid metal embrittlement of Zn-galvanised TWIP steel

Bertolo, Virgínia; Mahadevan, Gautham; Petrov, Roumen H.; Popovich, Vera

DOI
10.1016/j.jmrt.2025.08.097

Licence
CC BY

Publication date
2025

Document Version
Final published version

Published in
Journal of Materials Research and Technology

Citation (APA)
Bertolo, V., Mahadevan, G., Petrov, R. H., & Popovich, V. (2025). The role of microstructure in crack growth during liquid metal embrittlement of Zn-galvanised TWIP steel. *Journal of Materials Research and Technology*, *38*, 2569-2577. https://doi.org/10.1016/j.jmrt.2025.08.097

Journal of Materials Research and Technology 38 (2025) 2569–2577

Contents lists available at ScienceDirect

Journal of Materials Research and Technology

journal homepage: www.elsevier.com/locate/jmrt

The role of microstructure in crack growth during liquid metal embrittlement of Zn-galvanised TWIP steel

Virgínia Bertolo [a,b,*], Gautham Mahadevan [a,b], Roumen H. Petrov [b], Vera Popovich [a]

[a] *Department of Materials Science and Engineering, Delft University of Technology, Mekelweg 2, 2628 CN, Delft, the Netherlands*
[b] *Department of Electromechanical, Systems and Metals Engineering, Ghent University, Technologiepark 131, B-9052, Ghent, Belgium*

ARTICLE INFO

Handling Editor: SN Monteiro

Keywords:
Liquid metal embrittlement
Crack propagation
Microstructure
Zn-galvanised
TWIP steel

ABSTRACT

Improving the reliability of advanced high-strength steels (AHSS) for automotive applications requires a thorough understanding of liquid metal embrittlement (LME) crack propagation micromechanisms. This study investigates how microstructural features govern crack propagation paths in Zn-galvanised twinning-induced plasticity steel. LME was induced via Gleeble hot tensile tests at 800 °C, and a correlative analysis of the fracture surface's transversal plane revealed key crack-microstructure interactions. The results show that LME fracture is predominantly intergranular, preferentially occurring along high-angle, high-energy random grain boundaries (40°–56°). To quantify the effect of tensile stress on grain boundary segments, a normalised grain boundary stress factor was defined, ranging from 0 (no tensile stress, only shear) to 1 (pure tensile stress). Generally, high-angle grain boundaries require a stress factor below 0.2 for LME, while low-angle grain boundaries ($\theta < 15^\circ$) require at least 0.5. Most coincident site lattice boundaries between $\Sigma 5$ and $\Sigma 29$ are affected by LME, whereas $\Sigma 3$ boundaries remain resistant, even at high stress factor. However, cases where Zn penetration was absent despite high misorientation angles and stress factors, or where cracking occurred under the lowest stress factor (parallel to the loading axis), suggest additional, unidentified factors influence LME. These findings highlight the need for advanced three-dimensional modelling to capture the complex interaction between microstructure, stress state, and Zn penetration, not fully resolved in experiments. These insights could guide the development of LME-resistant steels, supporting their safe and reliable use in the automotive industry.

1. Introduction

Liquid metal embrittlement (LME) is a critical phenomenon affecting a wide range of solid–liquid metal systems (e.g., Fe–Zn, Ga–Al, Fe–Pb) during high-temperature processes across multiple sectors [1–4]. In particular, LME poses a major technological challenge to the implementation of advanced high-strength steels (AHSS) in the automotive industry. During vehicle assembly, resistance spot welding (RSW) is used to join components, exposing the material to localised fast, high-temperature heating at thousands of weld spots. This process generates steep thermal gradients and residual tensile stresses. LME arises during RSW when molten Zn – originating from the protective coating applied to automotive steels for corrosion resistance – interacts with the steel substrate under residual tensile stress, causing grain boundary decohesion and subsequent cracking. Among AHSS, austenite-containing grades exhibit the highest susceptibility to LME. In particular, fully austenitic twinning-induced plasticity (TWIP) steel has demonstrated pronounced sensitivity to LME, making it the focus of this study [2,5–7,8].

Understanding the LME micromechanisms is essential for controlling embrittlement and contributing to the broader adoption of AHSS in safety-critical applications. The microstructural mechanisms governing LME crack propagation have been widely studied [3,9,7,10,11–14]. While transgranular fracture has been observed to contribute to LME in ferritic grains, the phenomenon is predominantly intergranular [15,16]. This highlights the crucial role of grain boundary characteristics on LME crack growth. High-angle grain boundaries ($\theta > 15^\circ$), with their high atomic mismatch and high energy, are generally more prone to Zn penetration. In contrast, low-angle grain boundaries ($\theta < 15^\circ$) [9,7,11–13] and low-$\sum$ coincident site lattice (CSL) grain boundaries ($\sum \leq 29$), particularly twin $\sum 3$ ($\theta = 60^\circ$) boundaries, with a high atomic match and low energy, are considered more resistant to LME [10,11,12,14]. In a few studies, the susceptibility of grain boundaries to LME is also reported to depend on their alignment with the tensile loading axis [11,

---

* Corresponding author. Department of Materials Science and Engineering, Delft University of Technology, Mekelweg 2, 2628 CN, Delft, the Netherlands.
E-mail address: v.moretebarbosabertolo@tudelft.nl (V. Bertolo).

https://doi.org/10.1016/j.jmrt.2025.08.097
Received 26 May 2025; Received in revised form 6 August 2025; Accepted 13 August 2025

17–19]. A grain boundary is prone to LME when its alignment relative to the load component is sufficiently high compared to the boundary's cohesive strength [18]. The susceptibility of a grain boundary to LME increases as it becomes more perpendicular to the applied loading axis, since this orientation maximises the tensile stress component acting normal to the boundary [11,15,17]. On the other hand, grain boundaries parallel to the loading axis are observed not to participate in the embrittlement process [11,15,17,18]. These descriptors – grain boundary misorientation angle, grain boundary energy, and tensile loading component – are often treated as sufficient to justify broader conclusions, despite the complexity of the underlying micromechanisms [3,7,10,11,15]. This complexity is highlighted by the contradictory findings in studies that seek to understand the effect of microstructure on LME [3,7,11,20]. Razmpoosh et al. [11] report that for a Zn-galvanised 304 austenitic stainless steel, no LME has been observed through low-angle random and low-$\sum$ CSL grain boundaries assumed coherent even under maximum tensile loading component (grain boundary oriented perpendicularly to the applied load axis). Similarly, Hoagland and Hugo [3] and Hong et al. [20] observed that low-angle random and low-$\sum$ CSL have high resistance to LME in Ga–Al and Zn–Fe systems, respectively. Contrarily, Razmpoosh et al. [7] observed LME occurring through high-angle and $\sum 3$ CSL grain boundaries assumed incoherent in a Zn-galvanised TWIP steel. Another study by Ramzpoosh et al. [21] reports that the contribution of $\sum 5$–29 in LME in a 304 austenitic stainless steel to LME in a 304 austenitic stainless steel remains inconclusive, further underscoring that the influence of these boundaries on LME is not yet fully established and requires confirmation through follow-up studies.

The current understanding of LME remains incomplete, with limited and often inconclusive literature on the influence of critical grain parameters—particularly the role of CSL grain boundaries—on crack propagation. In this study, we adopt a similar framework, focusing on grain boundary misorientation and boundary alignment to the applied loading axis. However, our findings provide new insights by documenting cases that deviate from several theoretical expectations regarding the preferred crack propagation path during LME [3,7,11,15,17,18,20]. These observations indicate that two-dimensional analysis of grain boundary misorientation and alignment with the tensile axis alone are insufficient to fully explain the observed embrittlement behaviour, revealing inconsistencies and gaps that highlight the need to consider additional factors influencing crack growth. A lack of detailed understanding of the microstructural factors governing LME crack propagation hinders the development of effective mitigation strategies specifically tailored to TWIP steels. By identifying and analysing these deviations, our study offers clarifying evidence on the limitations of existing assumptions and proposes directions for refining mechanistic understanding.

This work quantitatively examines the influence of grain characteristics on LME crack growth paths in Zn-galvanised TWIP steel. Gleeble hot tensile tests were carried out to simulate the thermomechanical process of actual RSW leading to LME. Subsequently, the fracture's surface transversal plane was analysed to investigate the crack-microstructure interaction. Gaining deeper insights into these mechanisms will improve predictive modelling and support the design of steels with enhanced resistance to LME, ultimately supporting the reliable use of Zn-coated TWIP steels in automotive applications.

2. Materials and methods

The investigated material consists of fully austenitic twinning-induced plasticity (TWIP) steel sheets with a thickness of 1.23 mm. The commercial sheets were supplied in a hot-dip galvanised finish with a Zn coating layer averaging 12 ± 2 μm in thickness. Table 1 lists the chemical composition, average grain size (max ferret diameter with 15° tolerance angle, excluding coherent $\sum 3$ boundaries), and mechanical properties – yield strength (σ_Y), ultimate tensile strength (UTS), and uniform elongation (UE) of the TWIP steel.

Load-controlled hot tensile tests were performed via the Gleeble thermomechanical simulator, following the thermal profile in Fig. 1 (a). Tensile specimens (Fig. 1 (b)) are chemically etched in a 15 % HCl and 2 % hexamethylenetetramine solution to dezinc one or both sides – for single-sided and uncoated specimens, respectively –, with duct tape protecting the surface that is not to be exposed. Preliminary tests were carried out at 600 °C, 700 °C, and 800 °C in uncoated and single-sided Zn-coated tensile specimens to determine the temperature of the highest LME susceptibility. At 800 °C, the material exhibited the most significant ductility reduction, 80 % compared to an uncoated material tested under the same conditions. Hence, further investigations in this study focus on specimens tested at 800 °C. To assess the extent of the uniformly heated region for further investigations on crack propagation, thermocouples were positioned at the centre of the tensile specimen (control thermocouple) and at distances of 1 mm, 2 mm, and 3 mm from this reference point. The recorded temperature variations relative to the control thermocouple were 0 °C, 20 °C, and 60 °C, respectively. Based on these measurements and assuming a symmetrical temperature distribution on either side of the control thermocouple, the homogeneously heated zone was determined to span approximately 2 mm. Consequently, the analysis in this study focuses on this region. The temperature accuracy in the Gleeble experiments is estimated at ± 0.75 %.

To investigate the microstructural effects on LME crack growth and identify the critical features, the transverse section of fracture surfaces (Fig. 1 (c)) was studied. Samples were prepared metallographically by SiC grinding papers followed by polishing with 3 μm diamond suspension, 1 μm diamond suspension, and colloidal silica suspension (OPS). To assess potential crack propagation micromechanisms, the investigation was focused on regions where the crack opening was sufficiently narrow to allow alignment and correlation of microstructural features on both sides of the crack. This was feasible only in crack branches, as the main cracks exhibited large openings and significant material loss, which prevented reliable evaluation of the microstructural influence on the crack propagation path. Analyses were carried out through scanning electron microscopy (SEM), energy dispersive spectroscopy (EDS), and electron backscatter diffraction (EBSD). EBSD data was acquired on a Helios G4 PFIB SEM using a probe current of 3.2 nA and an accelerating voltage of 30 kV, a tilt angle of 70°, and a step size of 50 nm using TEAM-EDAX software in a hexagonal scan grid. The data was post-processed with EDAX-TSL-OIM Analysis TM v8 software. No cleanup procedure was required in the post-processing step. Grains were defined with a tolerance angle of 15° and a minimum size of 5 pixels, with multiple rows required. Taylor factor maps were generated for the 12 slip systems in FCC Fe, the critical resolved shear stress (CRSS) was set to the default value of 0.2, and the Cauchy strain tensor equal to 1, -0.5, and −0.5, corresponding to the uniaxial tensile axis along the A1 axis.

Table 1
Chemical composition, average grain size, and mechanical properties of the TWIP steel. σ_Y, UTS, and UE stand for yield strength, ultimate tensile strength, and uniform elongation, respectively.

Fe	C	Mn	Al	Ni	Cr, S, Si, Ti, P	Average grain Size (μm)	σ_Y (MPa)	UTS (MPa)	UE (%)
wt.%									
Bal.	0.62 ± 0.01	16.8 ± 0.3	1.30 ± 0.02	0.5 ± 0.01	0.24 ± 0.02	5.4 ± 1.7	435	900	54

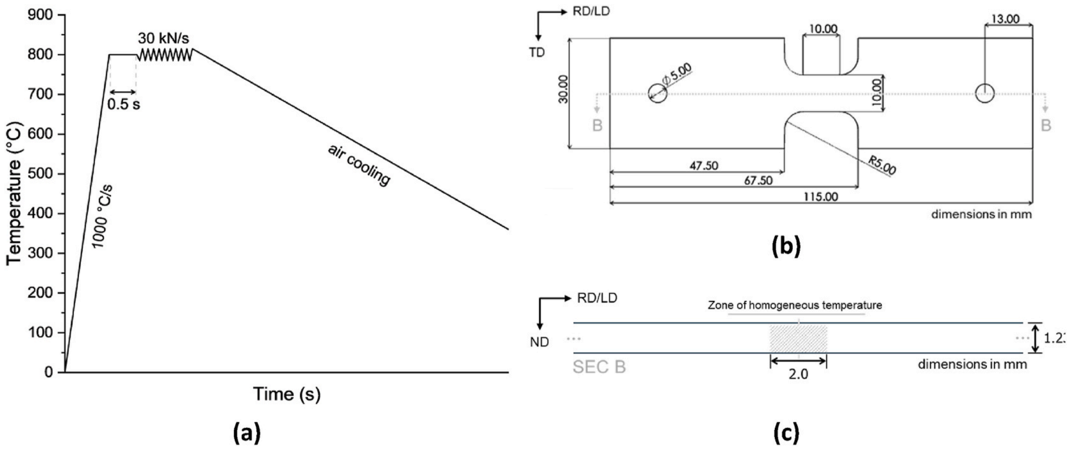

Fig. 1. Illustration of (a) Gleeble hot tensile specimens' dimensions and orientation, (b) analysed specimen's plane where the homogeneous heat-treated area is represented in grey and (c) Gleeble thermomechanical profile used in hot tensile tests. All dimensions are in mm. RD, LD, TD, and ND stand for rolling, loading, transverse, and normal direction, respectively.

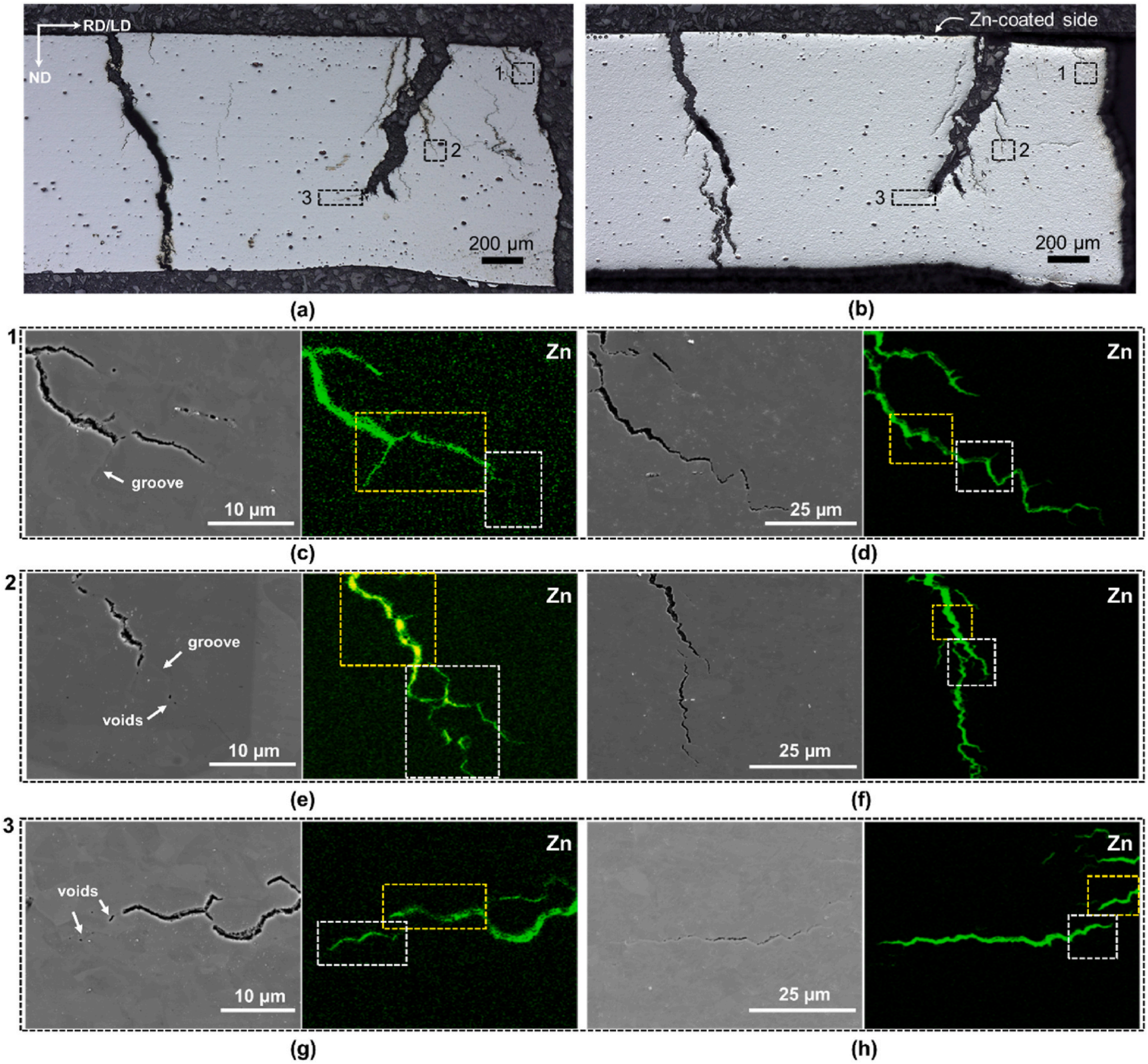

Fig. 2. SEM micrographs and Zn EDS maps at crack tips of specimens tested up to fracture (a) before and (b) after additional polishing Areas 1, 2, and 3 marked in (a) and (b) are shown in detail in (c), (e), and (g) and (d), (f), and (h), respectively. In (c), (e), and (g), yellow dashed rectangles mark visible crack tips before polishing, while dashed rectangles indicate Zn-enriched areas ahead of the crack. After repolishing, in (d), (f), and (h), yellow rectangles relocate the same regions before repolishing, and white dashed rectangles reveal subsurface cracks at locations previously shown only Zn enrichment and surface imperfection.

3. Results

Our initial SEM/EDS analysis of crack propagation paths revealed that surface observations alone can be misleading, as Zn enrichment along grain boundaries without a visible crack at the surface does not necessarily indicate solid-state Zn diffusion. The SEM micrographs and Zn EDS maps of three representative crack tips (location indicated in Fig. 2 (a)) are shown in more detail in Fig. 2(c)–(e), and (g). As shown in EDS maps, Zn is found inside and ahead of visible cracks. However, Zn traces at crack tips often appeared associated with surface imperfections such as grooves and voids, raising questions about whether the Zn signal indicated solid-solute Zn grain boundary diffusion or existing cracks filled with Zn beneath the observed surface. To investigate these hypotheses, the sample was slightly ground and polished to expose subsurface features. Fig. 2 (b) shows the newly revealed surface in the presence of new and pre-existing cracks. The previously analysed areas, i.e., Fig. 2(c)–(e), and (g), were located and re-analysed by EDS (Fig. 2 (d)–(f), and (h)). While slight changes in crack morphology occurred due to surface renewal, cracks maintained their predominant shape, enabling correlation between the initial Zn signals and ahead of the crack tip in the fresh surface. In Fig. 2(c)–(e), and (g), yellow dashed rectangles mark the location of visible crack tips before Zn-enriched zones associated with surface voids and grooves, and white dashed rectangles indicate areas ahead of the visible crack tips where Zn enrichment was detected. After repolishing (Fig. 2(d)–(f), and (h)), yellow rectangles help locate the same regions as before repolishing, while the white rectangles highlight subsurface cracks where only Zn enrichment and surface imperfections were previously observed, confirming that these Zn signals corresponded to underlying cracking. Further analysis revealed subsurface cracks, indicating that the Zn signal detected by EDS at this scale is not necessarily a sign of crack-free regions. In fact, it is observed that wherever a Zn signal is detected, a crack is associated with it. However, although there is a clear correlation between Zn presence and cracking, this does not imply direct causation in every case. The observed correlation may arise from the analysis spatial resolution and the fact that grain boundaries are much thinner than the electron interaction volume in EDS analysis, causing their signal to be heavily diluted by the surrounding matrix. Thus, when Zn is detectable at grain boundaries in this study, the local Zn concentration is high enough to overcome this dilution effect. This suggests a significant local enrichment that is likely sufficient to cause grain boundary decohesion and initiate cracks. For the purposes of this study – where the length scale is selected to allow a statistically meaningful representation of the crack path – future investigations of crack growth will use Zn EDS signals as indicators of preferential crack propagation paths.

The LME interplay with the TWIP steel microstructure has been studied through EBSD along different crack paths. The first analysis of the transverse fracture surface showed that LME on the investigated Zn-coated TWIP steel predominantly follows an intergranular fracture mode with scarce occurrence, i.e., about 3 %, of transgranular fracture through austenitic grains (Fig. 3). The transgranular fracture was confirmed by plotting IPF maps at different sample rotations, ND (Fig. 3 (a)), RD (Fig. 3(b)), and TD (Fig. 3(c)), and verifying that both sides of the grain maintain the same orientation. This approach is important because the grain orientation is dependent on the viewing direction and grains with different orientations can appear similar in one projection but differ in others. Therefore, using multiple orientations reduces the likelihood of mistaking two adjacent grains with similar colours for a single grain. 3D crystal lattice cubes are analysed in grains along the crack and reveal that the traces of {001} (Fig. 3(a), grain area 1) and {011} (Fig. 3(a), grain areas 2 and 3) planes are largely aligned with the fracture plane (within a tolerance angle of 15°).

Given the intergranular dominance, we further investigated the grain boundaries along the crack path, identifying those that serve as preferred and rejected trajectories for LME crack propagation. In the following analysis, we refer to grain boundaries with and without Zn. However, it should be noted that some grain boundaries categorised as "without/no Zn" may still exhibit negligible Zn diffusion that remains undetected by EDS, likely due to slower diffusion rates [3]. In such cases, these grain boundaries are not expected to contribute significantly to LME.

In total, 155 grain boundaries with Zn penetration and LME cracking and 80 without Zn were analysed (Fig. 4 (a)). The majority of grain boundaries associated with Zn penetration and LME cracking were high-angle boundaries (97 %), with nearly 50 % falling within a narrow misorientation angle range of 40°–56°. Similarly, most grain boundaries without Zn penetration and cracking were also high-angle (95 %), with approximately 50 % exhibiting misorientations between 54° and 60°. While these characteristics make both scenarios appear alike, the key distinction lies in the involvement of CSL grain boundaries, which play a critical role in determining Zn penetration and crack susceptibility. Around 15 % of the grain boundaries involved in LME embrittlement are

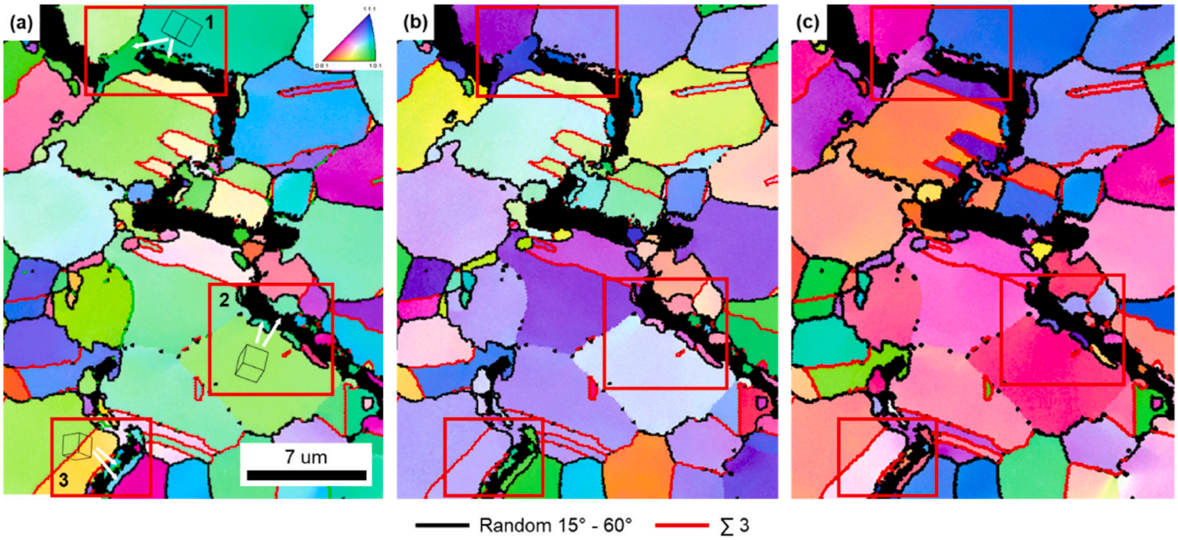

Fig. 3. IPF (a)-ND, (b) RD, and (c) TD maps of a transverse fracture surface showing predominantly intergranular LME crack with three transgranular areas, highlighted by red rectagles. 3D crystal lattice cubes illustrate the orientation of grains along the crack path. Black lines indicate random high-angle grain boundaries (15–60°), while red lines mark $\sum 3$ grain boundaries.

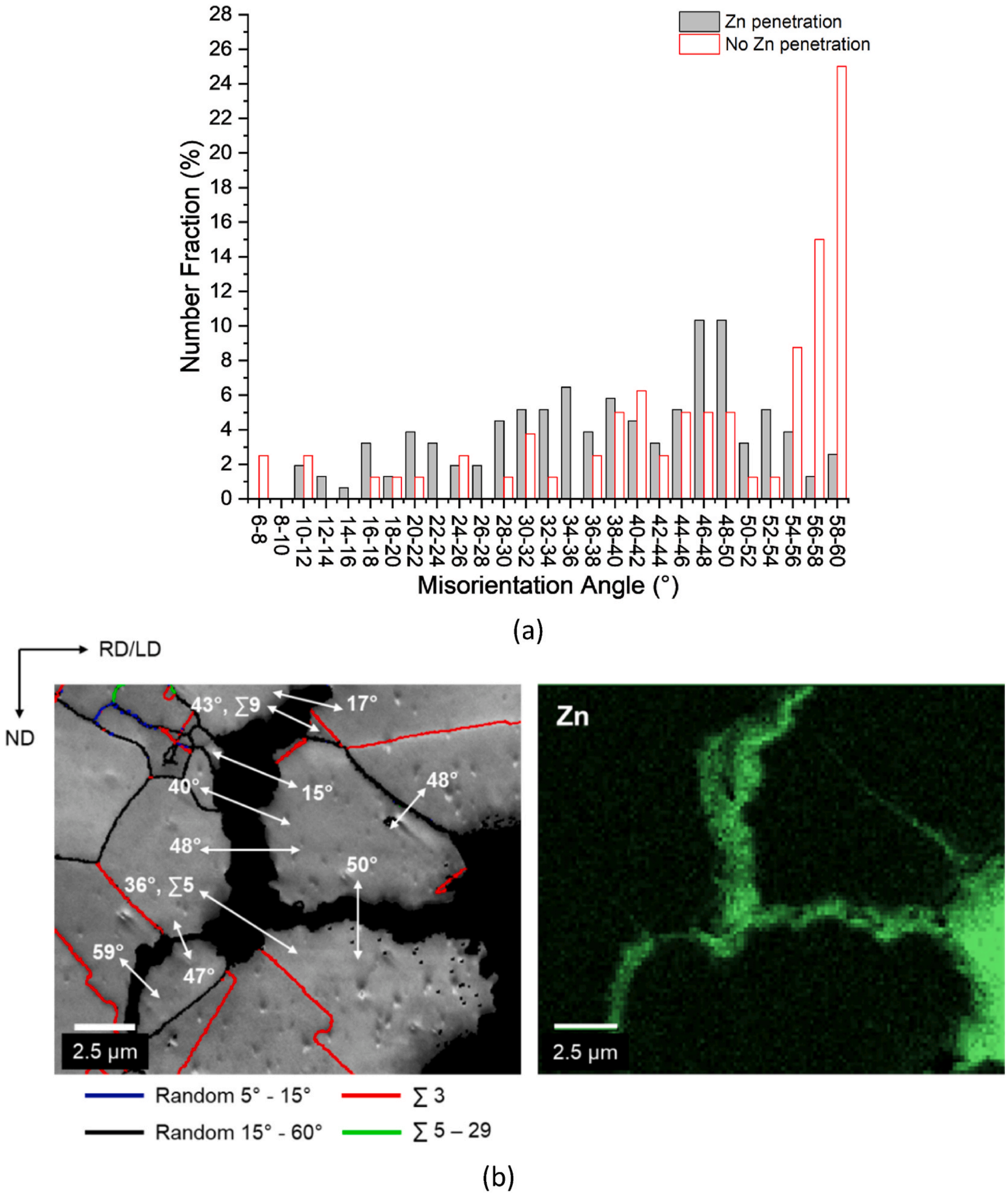

Fig. 4. (a) Misorientation angle distribution of grain boundaries with and without Zn penetration and (b) an EBSD grain boundary map and Zn EDS map from an analysed area. In (b), blue, black, red, and green lines represent random low-angle ($\theta < 15^\circ$), high-angle ($\theta \geq 15^\circ$), $\sum 3$, and $\sum 5$–29 grain boundaries, respectively.

CSL boundaries with Σ values of 5 or higher. In contrast, nearly 50 % of the grain boundaries on the rejected crack path are CSL grain boundaries, with 85 % having Σ3 misorientations. To visually complement the statistical distribution, Fig. 4 (b) shows a representative EBSD grain boundary map and Zn EDS map from the analysed area, where grain boundaries are colour-coded according to their misorientation angles. This provides spatial context for the distribution presented in Fig. 4 (a) and illustrates the typical arrangement of high- and low-angle boundaries as well as CSL grain boundaries within the microstructure.

Another key factor influencing Zn penetration and LME cracking in the studied TWIP steel is the tensile stress acting on grain boundary segments, which depends on the angle between the grain boundary and the loading direction. To quantify this effect, we define a normalised grain boundary stress factor, where the applied stress is maximum when the boundary is perpendicular to the loading direction (90°) and minimum when it is parallel (0°). The stress factor is determined by normalising the angle between the grain boundary and the horizontal loading axis relative to 90°, which represents the condition of maximum tensile stress. This factor ranges from 0, indicating no tensile stress (only shear), to 1, representing pure tensile stress. This normalisation provides a direct measure of the stress contribution based on grain boundary orientation, facilitating the analysis of its role in LME susceptibility. For this analysis, the data obtained from the 235 analysed grain boundaries were divided into 5 groups: 1) and 2) random boundaries with and without Zn penetration; 3) and 4) CSL boundaries with $\sum$ values between 5 and 29 with and without Zn penetration; and 5) $\sum 3$ CSL grain boundaries without Zn penetration. Fig. 5 exhibits the correlation between normalised grain boundary stress factors and misorientation angles for these groups.

For random grain boundaries, we observed that 80 % of the low-angle boundaries ($\theta < 15^\circ$) with Zn penetration have a normalised grain boundary stress factor of at least 0.5. In contrast, the unaffected

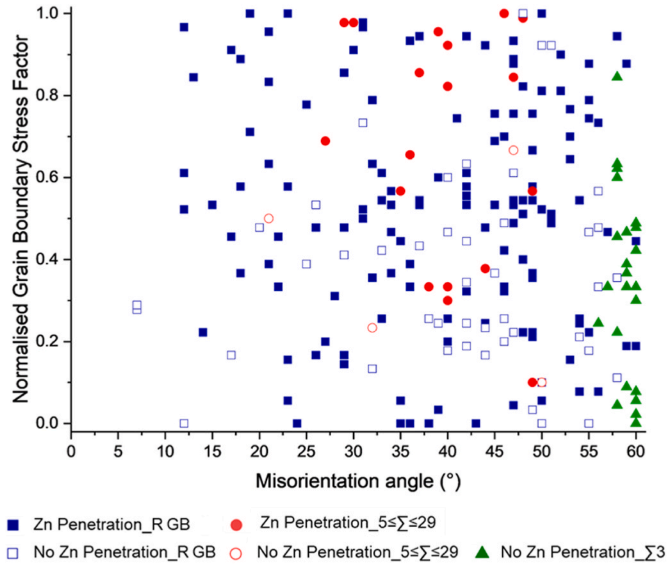

Fig. 5. Relationship between the normalised grain boundary stress factor (maximum (1) when the grain boundary is oriented perpendicular and minimum (0) when parallel to the loading direction) and misorientation angles for random grain boundaries with and without Zn penetration, CSL boundaries with ∑ values of 5–29 with and without Zn penetration, and ∑3 CSL boundaries without Zn penetration.

low-angle boundaries exhibited normalised grain boundary stress factors below 0.3. As can be seen in Fig. 5, the normalised grain boundary stress factor required for Zn penetration and cracking decreased with increasing misorientation angles, with a minimum normalised grain boundary stress factor, 0, required for misorientation angles from 24°. For CSL grain boundaries with Σ values between 5 and 29, 80 % experienced Zn penetration and cracking, but no clear trend in the required normalised grain boundary stress factor was observed. Additionally, Fig. 5 shows that no Σ3 grain boundary participated in Zn penetration and cracking, even under high-normalised grain boundary stress factors of 0.8.

Despite the general observations mentioned above, many Zn penetration pathways remain unclear. We estimate that almost 50 % of the grain boundaries that do not participate in LME would have favourable conditions for Zn penetration and cracking based on their misorientation angles and stress factor. One can see in Fig. 5 that, for certain misorientation angles, some grain boundaries with a more favourable normalised grain boundary stress factor (above 0.5) — expected to promote LME — do not exhibit cracking. In contrast, others with a lower normalised grain boundary stress factor do. Furthermore, even at very similar misorientation angles and normalised grain boundary stress factors, LME susceptibility varies between grain boundaries. Illustrative examples are presented in Fig. 6. In Fig. 6 (a), in area 1, we see that Zn penetrates through a 40°, 0.2 grain boundary while, in area 2, similar grain boundaries, 44°, 0.2 and 39°, 0.2 are not filled with Zn. In Fig. 6 (b), areas 2 and 3 show that Zn penetration gets interrupted when encountering a similar misorientation angle with a higher normalised grain boundary stress factor (47°, 0–46°, 0.5) and larger misorientation with the same normalised grain boundary stress factor (31°, 0.5–47°, 0.5). Lastly, 7 % of the grain boundaries involved in Zn penetration and

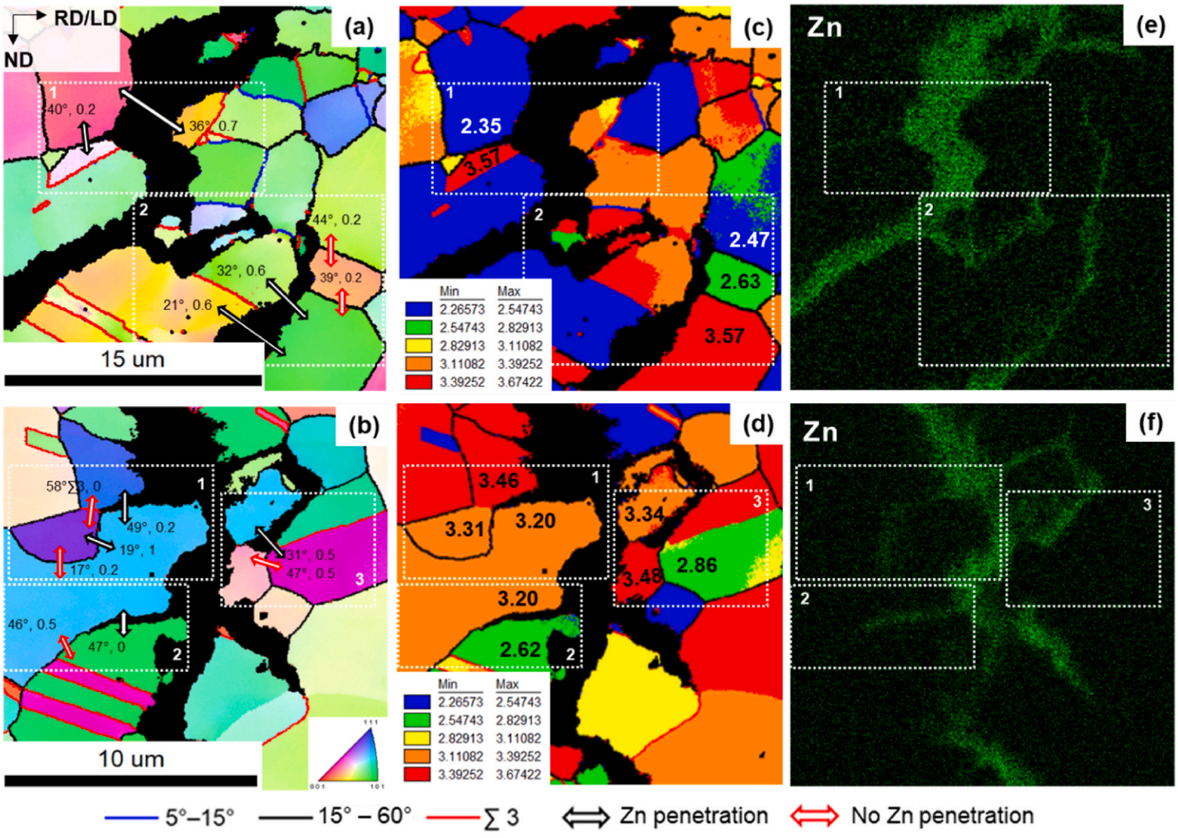

Fig. 6. EBSD (a, b) IPF-ND, (c,d) Taylor factor map, and (e,f) Zn EDS maps, where we investigate the preferred and rejected trajectories for LME crack propagation in the fractured specimen. In (a,b), misorientation angles and normalised grain boundary stress factors of grain boundaries used as examples are shown. Red arrows indicate grain boundaries that had Zn penetrated through and black arrows identify the ones that Zn did not penetrate through. In (c,d), the numbers inside certain grains used as examples indicate their absolute Taylor factor. In (a–d), blue, black, and red lines represent random low-angle ($\theta < 15°$), high-angle ($\theta \geq 15°$) and ∑ 3 grain boundaries, respectively.

LME cracking have been aligned nearly parallel to the loading direction (normalised grain boundary stress factor<0.1), e.g., Fig. 6 (b), area 2. These findings contradict theoretical expectations where interruption of LME is expected at low-angle random grain boundaries, $\Sigma < 29$ CSL grain boundaries, and grain boundaries aligned parallel to the tensile loading axis [11,15,17].

4. Discussion

To better understand the predominant fracture mechanism, we now focus on the intergranular crack propagation, where grain boundary type and normalised grain boundary stress factors act as key features influencing the LME crack growth path. High-angle grain boundaries, mostly between 40° and 56°, have a marked propensity for grain boundary penetration and cracking. This finding aligns with previous studies that underscore the susceptibility of high-angle grain boundaries in LME due to their high energy [9,7,11,22]. Regarding CSL grain boundaries, we observed that Σ3 grain boundaries have not participated in Zn penetration and cracking, demonstrating their exceptional effectiveness in hindering crack propagation in the studied TWIP steel. On the other hand, grain boundaries with larger Σ values, between 5 and 29, were found to play a role in LME. This is attributed to CSL Σ3 grain boundaries having the highest symmetry and, consequently, lower free volume and free energy, being less favourable for Zn penetration. In this regard, the literature is contrary to the findings of this study [7,11]. Razmpoosh et al. [11] reported that CSL grain boundaries with Σ values lower than 29 do not trigger LME even at the maximum normalised grain boundary stress factor. Hoagland and Hugo [3] and Hong et al. [20] also observed that $\sum<29$ have high resistance to LME in Ga–Al and Zn–Fe systems, respectively. Another study from Razmpoosh [7] concluded that Σ3 grain boundaries can play a role in LME due to the high fraction of grain boundaries with 60° misorientation, which Zn penetrated. Concerning the normalised grain boundary stress factor, the lower energy associated with low misorientation angles requires a greater normalised grain boundary stress factor. In this case, larger normalised grain boundary stress factors lead to a larger grain-boundary free volume for Zn to penetrate and crack to open, facilitating Zn penetration and ultimately leading to crack formation. However, counterintuitively, in a few cases, grain boundaries nearly parallel to the loading direction were observed to have Zn penetrated, resulting in cracking. During hot tensile tests, these grain boundaries are under shear and compressive stresses, meaning that they promote less atomic decohesion and, thus, are less conducive to crack opening and propagation than grain boundaries that are more misoriented to the loading direction. This finding contrasts with a study by Bhattacharya et al. [15] that claims that grain boundaries rich in Zn, when aligned parallel to the loading direction, do not crack and are resistant to LME. Other unclear Zn penetration pathways were observed, suggesting additional factors may influence LME in this system.

Beyond misorientation angles and stress factors, we investigated additional microstructural factors that could influence grain boundary susceptibility to Zn penetration. The stress and strain state of grain boundaries has been shown to affect penetration behaviour [23,24]. For instance, Connoley [24] states that in the case of heterogeneous deformation in an IN718 tested during high-temperature low-cycle fatigue, intense slip lines generate stress concentrations at grain boundaries, which enhance oxygen diffusivity, promoting its fast transport. Hence, we further investigated the role of grain boundary stress and strain in Zn penetration. In polycrystalline materials, each grain has a distinct crystal orientation, which leads to unique yield characteristics. Consequently, grains with different crystallographic orientations deform differently under applied stress, creating strain incompatibilities at their interface [25]. When a grain undergoes plastic deformation via dislocation slip, strain incompatibility may prevent dislocations from transmitting into the adjacent grain. This leads to dislocation pile-ups at the grain boundary, generating stress concentrations [26]. The Taylor factor quantifies how grains accommodate deformation based on their crystallographic orientation relative to the applied stress [27]. By analysing the Taylor factors of grains along the unclear LME cracking path, we can assess whether strain incompatibility contributes to LME susceptibility. Fig. 6 (c) and (d) show the Taylor factor maps of two representative LME crack propagation paths. In addition, absolute Taylor factors of grains involved in unclear LME paths are indicated. In Fig. 6 (d), the grain boundary in area 1, where Zn penetration occurs, exhibits a higher Taylor factor difference (1.22) compared to the grain boundaries in area 2, where no Zn penetration is observed (0.16 and 0.94). Conversely, another grain boundary without Zn penetration in Fig. 6(d) has a higher Taylor factor difference (0.62) than the Zn-penetrated grain boundaries (0.26 and 0.11 in area 1, 0.58 in area 2, and 0.48 in area 3). Furthermore, despite the grain boundary in area 3 having a similar Taylor factor difference (0.62 vs. 0.58), the same misorientation angle (47°), and a higher stress factor (0.5 vs. 0) compared to area 2, Zn preferentially penetrates through the grain boundaries in area 2. This suggests that strain incompatibility is not a determining factor in the LME crack path in this system.

In addition to the microstructural and stress factors analysed and mentioned above, the chemical composition of the steel may also influence Zn penetration and likely crack path selection during LME. Studies [28,29] in the literature observe that alloying elements can affect grain boundary cohesion, solute segregation, and Zn diffusivity. For example, Abdiyan et al. [28] reported that the addition of 0.2 wt% of Mo increased LME susceptibility in a quenched and partitioned advanced high-strength steel by enhancing B segregation at prior austenite grain boundaries, which improved boundary cohesion and delayed crack initiation. Similarly, Colburn, Speer, and Klemm-Toole [29] observed that a higher Al content reduces Zn solubility and diffusivity in a quenched and partitioning steel substrate, thereby mitigating LME susceptibility. As TWIP steels are highly alloyed, their chemical composition may influence Zn diffusion behaviour, segregation dynamics, and consequently the energy barrier for crack propagation along specific grain boundaries. The compositional factor likely adds to the complexity of crack path selection mechanisms in TWIP steels. While this manuscript focused primarily on crystallographic and stress factors, a deeper analysis of local chemical composition and segregation behaviour is necessary to clarify if the chemical composition may be playing a role in LME, particularly in some of the unclear findings regarding crack path deviations observed in this study. This is an important aspect for future investigations.

Although LME in the studied Zn-galvanised TWIP steel predominantly exhibits intergranular characteristics, 3 % of the crack trajectory is transgranular. While rarely observed and, thus, not significant to contribute to the final LME fracture, the transgranular fracture of austenite in Zn-assisted LME deserves attention as it has not been previously reported in the literature. From a crystallographic perspective, the observed transgranular cracks propagate through grains oriented along {001} and {011} planes. This is particularly intriguing because, in austenite, {111} planes typically exhibit the lowest surface energy, making them more susceptible to cleavage fracture [30]. Furthermore, previous studies have shown that Zn atoms preferentially segregate to {111} and {001} planes [30], which would favour these planes for embrittlement and crack propagation. However, the observation of transgranular cracking through {011} planes in this study suggests that crystallographic surface energy and segregation tendencies alone cannot fully explain the transgranular crack path selection.

Bhattacharya et al. [15] observed transgranular and intergranular LME cracking through ferritic grains, while austenite only participated in intergranular cracking in a Zn-galvanised AHSS. The authors [15] attribute the transgranular fracture through ferritic grains to the combination of two factors. First, the adsorption of liquid Zn atoms onto the crack tip at the steel substrate, following the Stoloff-Johnson-Westwood-Kamdar (SJWK) mechanism [31,32], along with the bulk diffusion of Zn from liquid Zn at grain boundaries [15].

Both processes can weaken the atomic Fe–Fe bonds, reducing the critical stress for cleavage fracture and facilitating transgranular cracking. Second, the unfavourable microstructure at the crack tip, where a grain boundary oriented parallel to the load direction had insufficient tensile stress to fracture, causing the intergranular crack to propagate transgranularly instead. In our study, the EDS maps in Fig. 6 show that the Zn signal is confined to the crack path and grain boundaries, indicating that long-range bulk diffusion is unlikely to be the primary cause of the observed transgranular fracture in the investigated steel. Instead, the fracture mechanism is more likely driven by the adsorption of liquid Zn atoms at the crack tip, aligning with the SJWK micromechanism. Moreover, as can be seen in Fig. 7, in our study, the grain boundaries at the crack tips preceding transgranular fracture (highlighted by the white dashed ellipse) are not aligned parallel to the loading direction. Instead, as suggested by the results in Fig. 5, they are likely oriented in a way that favours the continuation of intergranular fracture (Fig. 7).

Overall, our findings demonstrate that while misorientation angles and tensile stress factor significantly influence the LME crack propagation path in Zn-galvanised TWIP steel, they alone cannot fully account for the preferential fracture trajectories observed. The role of Zn penetration appears to be governed by additional, not yet identified, factors contributing to the complexity of the LME phenomenon. One such factor could be the influence of the steel's chemical composition. The chemical composition of the steel substrate has been observed to affect Zn diffusion behaviour and segregation dynamics at grain boundaries [28,29]. As TWIP steels are highly alloyed, their chemical composition may have a strong influence on LME embrittlement. As a consequence, the local energy barriers for crack propagation along grain boundaries may be modified, and transgranular fracture can become more favourable than intergranular fracture along certain boundaries. To further clarify these interactions, advanced characterisation techniques such as Atom Probe Tomography (APT) are suggested, as they could provide direct insights into elemental segregation at grain boundaries, primarily the ones in unclear crack paths, at the atomic scale. Another key limitation of the current approach is its neglect of the three-dimensional microstructural context in which these boundaries exist. In practice, the surrounding grains can significantly affect local stress states by constraining or promoting deformation. This interaction is particularly critical in LME, where local grain-scale stress variations can affect Zn penetration behaviour and, consequently, crack path evolution. Even if such analyses were extended to include three-dimensional experimental techniques, they would likely still fall short of capturing the full contribution of neighbouring grains to local stress redistribution. A more comprehensive understanding would require three-dimensional modelling, such as the combination of phase-field modelling and finite element simulations capable of incorporating microstructure-mechanical interactions (e.g., grain orientations, grain boundary properties, diffusion, and stress), allowing for crack propagation simulation. However, such simulations demand high-resolution microstructural input, detailed orientation-dependent material properties, and significant computational resources. Moreover, coupling mechanical and diffusion phenomena adds another layer of difficulty, particularly in light of the limited availability of experimental data for validation at the microscale. While these challenges fall beyond the scope of the present work, they highlight important directions for future research.

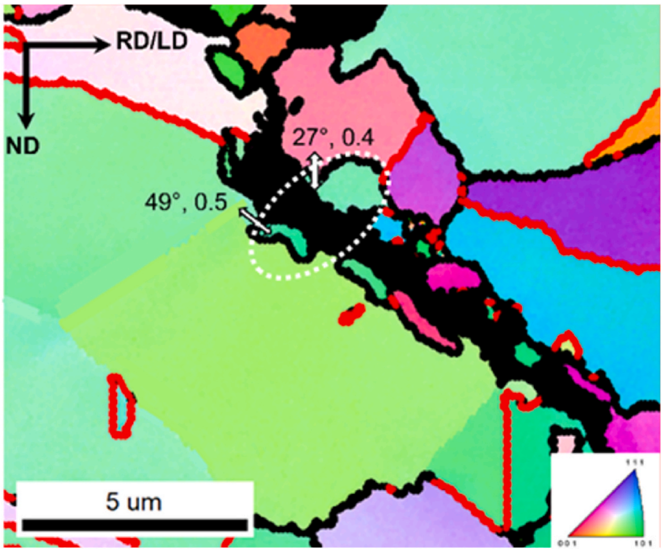

Fig. 7. IPF-ND of an area containing transgranular fracture, which is highlighted by the white dashed ellipse. Misorientation angles and normalised grain boundary stress factors of grain boundaries before transgranular fracture are indicated. Black and red lines represent random high-angle ($\theta \geq 15°$) and $\sum 3$ grain boundaries, respectively.

5. Conclusions

Gleeble hot tensile tests were performed on a Zn-galvanised TWIP steel at 800 °C, and the microstructural analysis of the fracture surface's transverse section revealed the influencing factors on LME crack propagation. Based on our findings, the following conclusions can be drawn.

1. Zn-assisted LME fracture is predominantly intergranular but not exclusively. A minor fraction (about 3 %) of cracks propagated transgranularly through austenitic grains primarily along {001} and {011} planes, indicating that alternative crack growth mechanisms can occasionally occur.
2. LME preferentially occurs along high-angle boundaries, with about 50 % of cracked boundaries having misorientation angles between 40° and 56°. In general, high-angle grain boundaries require a normalised grain boundary stress factor lower than 0.2 for LME. Nevertheless, a minimum normalised grain boundary stress factor (0, parallel to the loading axis) is observed to be sufficient for LME in some cases where misorientation angles are above 24°. Low-angle grain boundaries ($\theta < 15°$) also participated in LME, provided the normalised grain boundary stress factor is at least 0.5.
3. CSL grain boundaries exhibit varying resistance to LME. Most CSL grain boundaries with Σ values between 5 and 29 are susceptible to Zn diffusion and cracking, but no clear trend was observed in their dependence on the normalised grain boundary stress factor. In contrast, $\Sigma 3$ grain boundaries demonstrate complete resistance to Zn penetration and cracking, even under high-normalised grain boundary stress factors of 0.8, effectively hindering LME.
4. While misorientation angles and normalised grain boundary stress factors play a significant role, they do not fully explain all observed crack propagation paths. For instance, some high-angle grain boundaries with high stress factors remained unaffected, while others exhibited Zn penetration even under minimal tensile stress, such as boundaries parallel to the loading direction. These observations indicate that additional factors, such as local chemistry and grain boundary atomic structure, also contribute to LME, though these could not be directly resolved within the scope of this study.

This study challenges conventional assumptions and offers new insights into the intricate interplay between grain boundary characteristics and LME mechanisms, thereby advancing our understanding of LME crack propagation in Fe–Zn systems. By critically examining the limitations of commonly adopted analytical approaches, the work reveals a significant gap in current knowledge, particularly regarding the influence of surrounding grains and the factors governing Zn penetration. While the experimental results provide valuable information, they also underscore the complexity of the phenomenon and the limitations of two-dimensional analysis in capturing the full picture. Our findings indicate that misorientation angles, grain boundary energy, and normalised grain boundary stress factors are not able to fully explain the observed crack propagation paths. To address this, future efforts must involve a combined experimental–computational approach, integrating advanced finite element and phase-field modelling and atomistic-scale simulations such as first-principles calculations and molecular dynamics modelling with high-resolution three-dimensional microstructural characterisation. Although such modelling lies beyond the scope of the present work, the findings laid out here establish a foundation for future investigations aimed at developing more effective strategies to mitigate LME in advanced high-strength steels.

CRediT authorship contribution statement

Virgínia Bertolo: Conceptualization, Methodology, Validation, Formal analysis, Investigation, Resources, Data curation, Writing – original draft, Writing – review & editing. **Gautham Mahadevan:** Conceptualization, Writing – review & editing. **Roumen H. Petrov:** Conceptualization, Validation, Writing – review & editing, Supervision. **Vera Popovich:** Conceptualization, Validation, Writing – review & editing, Supervision, Project administration.

Data availability statement

The raw/processed data required to reproduce these findings cannot be shared at this time as the data also forms part of an ongoing study.

Declaration of competing interest

The authors declare that they have no known competing financial interests or personal relationships that could have appeared to influence the work reported in this paper.

Acknowledgement

This publication is part of the project N19010 in the Partnership Program of the Materials Innovation Institute M2i framework, which is partly financed by the Dutch Research Council (NWO) and the partners Tata Steel and AutomotiveNL.

References

[1] Jung G, Woo IS, Suh DW, Kim S-J. Liquid Zn assisted embrittlement of advanced high strength steels with different microstructures. Met Mater Int 2016;22:187–95. https://doi.org/10.1007/s12540-016-5579-7.
[2] Béal C. Mechanical behaviour of a new automotive high manganese TWIP steel in the presence of liquid zinc n.d.
[3] Hugo RC, Hoagland RG. The kinetics of gallium penetration into aluminum grain boundaries in situ observations and atomistic models n.d.
[4] Monchoux JP, Rabkin E. Microstucture evolution and interfacial properties in the Fe–Pb system. Acta Mater 2002;50:3161–76. https://doi.org/10.1016/s1359-6454(02)00129-5.
[5] Kang H, Cho L, Lee C, De Cooman BC. Zn penetration in liquid metal embrittled TWIP steel. Metall Mater Trans A 2016;47:2885–905. https://doi.org/10.1007/s11661-016-3475-x.
[6] Jung G. Liquid metal embrittlement of high Mn TWIP steel. Graduate Institute of Ferrous Technology, POSTECH; 2015.
[7] Razmpoosh MH, Biro E, Chen DL, Goodwin F, Zhou Y. Liquid metal embrittlement in laser lap joining of TWIP and medium-manganese TRIP steel: the role of stress and grain boundaries. Mater Char 2018;145:627–33. https://doi.org/10.1016/j.matchar.2018.09.018.
[8] Hong S-H, Kang J-H, Kim D, Kim S-J. Si effect on Zn-assisted liquid metal embrittlement in Zn-coated TWIP steels: Importance of Fe-Zn alloying reaction. Surf Coat Technol 2020;393:125809. https://doi.org/10.1016/j.surfcoat.2020.125809.
[9] Bhattacharya D, Cho L, Van Der Aa E, Pichler A, Pottore N, Ghassemi-Armaki H, et al. Influence of the starting microstructure of an advanced high strength steel on the characteristics of Zn-Assisted liquid metal embrittlement. Mater Sci Eng, A 2021;804:140391. https://doi.org/10.1016/j.msea.2020.140391.
[10] Tumuluru M. Effect of silicon and retained austenite on the liquid metal embrittlement cracking behavior of GEN3 and high-strength automotive steels. Weld J 2019;98:351s. https://doi.org/10.29391/2019.98.029. 64s.
[11] Razmpoosh MH, Macwan A, Goodwin F, Biro E, Zhou Y. Role of random and coincidence site lattice grain boundaries in liquid metal embrittlement of iron (FCC)-Zn couple. Metall Mater Trans A 2020;51:3938–44. https://doi.org/10.1007/s11661-020-05857-3.
[12] Oddershede J, Sun J, Gueninchault N, Bachmann F, Bale H, Holzner C, et al. Non-destructive characterization of polycrystalline materials in 3D by laboratory diffraction contrast tomography. Integrating Mater Manuf Innov 2019;8:217–25. https://doi.org/10.1007/s40192-019-00135-6.
[13] Razmpoosh MH, Langelier B, Marzbanrad E, Zurob HS, Zhou N, Biro E. Atomic-scale investigation of liquid-metal-embrittlement crack-path: revealing mechanism and role of grain boundary chemistry. Acta Mater 2021;204:116519. https://doi.org/10.1016/j.actamat.2020.116519.
[14] Razmpoosh MH, Macwan A, Goodwin F, Biro E, Zhou Y. Crystallographic study of liquid-metal-embrittlement crack path. Mater Lett 2020;267:127511. https://doi.org/10.1016/j.matlet.2020.127511.
[15] Bhattacharya D, Cho L, Van Der Aa E, Ghassemi-Armaki H, Pichler A, Findley KO, et al. Transgranular cracking in a liquid Zn embrittled high strength steel. Scr Mater 2020;175:49–54. https://doi.org/10.1016/j.scriptamat.2019.09.006.
[16] Ling Z, Wang M, Kong L, Chen K. Towards an explanation of liquid metal embrittlement cracking in resistance spot welding of dissimilar steels. Mater Des 2020;195:109055. https://doi.org/10.1016/j.matdes.2020.109055.
[17] Luithle A, Pohl M. On the influence of cold deformation on liquid metal embrittlement of a steel in a liquid zinc bath. Mater Corros 2015;66:1491–7. https://doi.org/10.1002/maco.201508344.
[18] Gong X, Marmy P, Volodin A, Amin-Ahmadi B, Qin L, Schryvers D, et al. Multiscale investigation of quasi-brittle fracture characteristics in a 9Cr–1Mo ferritic–martensitic steel embrittled by liquid lead–bismuth under low cycle fatigue. Corros Sci 2016;102:137–52. https://doi.org/10.1016/j.corsci.2015.10.003.
[19] Gong X, Marmy P, Qin L, Verlinden B, Wevers M, Seefeldt M. Effect of liquid metal embrittlement on low cycle fatigue properties and fatigue crack propagation behavior of a modified 9Cr–1Mo ferritic–martensitic steel in an oxygen-controlled lead–bismuth eutectic environment at 350 °C. Mater Sci Eng, A 2014;618:406–15. https://doi.org/10.1016/j.msea.2014.09.003.
[20] Hong S-H, Eo D-R, Lee S, Cho J-W, Kim S-J. Strong resistance to Zn-assisted liquid metal embrittlement of austenitic-TWIP/martensitic-HSLA multi-layered steel sheets additively manufactured by laser cladding. Acta Mater 2023;258:119224. https://doi.org/10.1016/j.actamat.2023.119224.
[21] Razmpoosh MH, Macwan A, Goodwin F, Biro E, Zhou Y. Suppression of liquid-metal-embrittlement by twin-induced grain boundary engineering approach. Materialia 2020;11:100668. https://doi.org/10.1016/j.mtla.2020.100668.
[22] Ludwig W, Pereiro-López E, Bellet D. In situ investigation of liquid Ga penetration in Al bicrystal grain boundaries: grain boundary wetting or liquid metal embrittlement? Acta Mater 2005;53:151–62. https://doi.org/10.1016/j.actamat.2004.09.012.
[23] Ghonem H, Zheng D. Depth of intergranular oxygen diffusion during environment-dependent fatigue crack growth in alloy 718. Mater Sci Eng, A 1992;150:151–60. https://doi.org/10.1016/0921-5093(92)90107-C.
[24] Connolley T. Initiation and growth of short cracks in U-Notch Bend specimens of supperalloy IN718 during high temperature low cycle fatigue n.d.
[25] Chen J, Furushima T. Effects of intergranular deformation incompatibility on stress state and fracture initiation at grain boundary: experiments and crystal plasticity simulations. Int J Plast 2024;180:104052. https://doi.org/10.1016/j.ijplas.2024.104052.
[26] Spearot DE, Sangid MD. Insights on slip transmission at grain boundaries from atomistic simulations. Curr Opin Solid State Mater Sci 2014;18:188–95. https://doi.org/10.1016/j.cossms.2014.04.001.
[27] Sarma GB, Dawson PR. Effects of interactions among crystals on the inhomogeneous deformations of polycrystals. Acta Mater 1996;44:1937–53. https://doi.org/10.1016/1359-6454(95)00309-6.
[28] Abdiyan F, McDermid JR, Okigami F, Pourbahari B, Macwan A, Saenz De Miera M, et al. Effect of Mo addition on the susceptibility of advanced high strength steels to liquid metal embrittlement. Materials 2025;18:1291. https://doi.org/10.3390/ma18061291.
[29] Colburn J, Speer JG, Klemm-Toole J. Effect of substrate Al content on liquid metal embrittlement susceptibility in quench and partitioned steels. Mater Sci Eng, A 2025;922:147636. https://doi.org/10.1016/j.msea.2024.147636.
[30] Chen Y, Wang C, Xu W. Effect of solutes on the performance of Zn-coating and Zn-inducing transgranular cracking in steel based on DFT calculations. J Mater Res Technol 2022;21:1519–27. https://doi.org/10.1016/j.jmrt.2022.09.124.
[31] Stoloff NS, Johnston TL. Crack propagation in a liquid metal environment. Acta Metall 1963;11:251–6. https://doi.org/10.1016/0001-6160(63)90180-9.
[32] Westwood ARC, Kamdar MH. Concerning liquid metal embrittlement, particularly of zinc monocrystals by mercury. Philos Mag 1963;8:787–804. https://doi.org/10.1080/14786436308213836.